



Investigation into the contact characteristics of rough surfaces with surface tension

Ling Li¹ · Qiang-Qiang Yun¹ · Hai-Fei Tian¹ · An-Jiang Cai¹ · Chang-Yong Cao²

Received: 29 December 2018 / Accepted: 24 July 2019
© The Brazilian Society of Mechanical Sciences and Engineering 2019

Abstract

Surface tension is a kind of force that exists between the molecules of the material surface, which has a significant influence on the contact characteristics of rough surfaces. Therefore, the Nayak's random process model is introduced to describe the height and curvature distribution of asperity on isotropic rough surfaces, and a single conical asperity system considering surface tension is established. Then, the single conical asperity system is extended to the entire rough surface, and a new contact model of the rough surface is presented based on statistical methods. The contact stiffness from the proposed model is added to the finite element model for comparison with experimental results. The effects of surface tension and semi-cone angle of conical asperity on the contact load, the contact area, and the contact stiffness of rough surfaces are revealed. The results show that the new model has larger normal load and contact stiffness, and a smaller real contact area than the classical elastic model where the dimensionless separation is constant. In addition, the contact load and contact stiffness between rough surfaces increase with increasing surface tension, but the real contact area decreases. When the surface tension is constant, the larger the semi-cone angles of the conical asperity, the greater the load, the real contact area, and the stiffness will be.

Keywords Conical asperity · Rough surface · Surface tension · Contact stiffness

1 Introduction

The joint surface which can be in general equivalent to the contact of two rough surfaces of mechanical structures has a great impact on the overall performance of the system. The study indicates that the real contact area between rough surfaces only accounts for 1–2% of the nominal contact area with the application of 100 MPa contact pressure on the surface, and the contact area is discontinuous [1, 2]. This discontinuous contact condition has a significant effect on the friction, wear, lubrication, and heat transfer characteristics of rough surfaces. Therefore, the contact behavior between

rough surfaces is a key factor affecting the contact characteristics of joint surfaces.

Extensive research has been conducted all over the world on the contact behavior between rough surfaces. Greenwood et al. [3] proposed that the height of the asperity on the machined surface can be approximated in a Gaussian distribution, forming the GW contact model. Chang et al. [4] presented the CEB model based on the conservation principle and studied the elastic and plastic deformation of the asperity. However, the elastic–plastic deformation of the asperity is ignored in the CEB model, and the contact load changed abruptly at the critical yield point. Based on fractal theory, a fractal contact model of the rough surface is established, but this model also ignored the elastic–plastic deformation of the asperity [5]. They considered that the critical contact area of the asperity is independent in size. The results show that the deformation process of the asperity does not conform to the traditional analysis results. To solve this problem, Yuan et al. [6] proposed a modified contact fractal model, concluding that as contact load gradually increases, the asperity will follow the deformation process of elastic deformation, complete plastic deformation and elastic–plastic deformation. Sepehri and Farhang

Technical Editor: Paulo de Tarso Rocha de Mendonça, Ph.D.

✉ Ling Li
liling@xauat.edu.cn

¹ School of Mechanical and Electrical Engineering, Xi'an University of Architecture and Technology, Xi'an 710055, China

² Laboratory for Soft Machines and Electronics, School of Packaging, Department of Mechanical Engineering, Michigan State University, East Lansing, MI 48824, USA

[7] considered the lateral contact between the asperity and the contact deformation of the asperity at different contact positions for deduction, which was more reasonable. Gorbatiikh et al. [8] studied the tangential energy consumption of the asperity when two rough surfaces were applied with tangential excitation forces.

Recent researches have shown that surface tension plays a crucial role in micro/nanosized contact [9–12], but was not considered in all the above micro-contact models for simulating the contact behavior of rough surfaces. Many scholars have studied extensively the influence of surface effects on contact problems. As early as 1975, the surface elasticity theory proposed by Gurtin et al. [13] laid a firm foundation for predicting the influence of surface tension on the contact characteristics of rough surfaces. Hajji [14] presented an analysis of the elastic deformation caused by a concentrated normal force acting on a homogeneous isotropic elastic half space with a constant surface tension and found that the deformation under the influences of surface tension obviously differs from the classical solution. Based on the surface elasticity theory, the two-dimensional and three-dimensional surface Green's functions of the elastic half space are derived, respectively [15, 16]. Cuenot et al. [17] studied the influence of surface tension on the mechanical properties of nanomaterials and pointed out that the increase in elastic modulus for the smaller diameters is due to the effect of surface tension. Considering the influence of surface stress on nano-sized problems, Wang et al. [18] researched the effects of surface stresses on contact mechanics by applying a concentrated force on an elastic half space with surface tension and pointed out that the maximum normal contact stress depends largely on the surface stress. Olsson and Park [19] developed a theoretical model for analyzing the flexural rigidity of nanowires, which takes into account the influences of both surface stress and surface elasticity based on three-dimensional elasticity theory. In addition, Gao et al. [20] first compared the effects of surface tension and surface elasticity on contact problems and found that the surface tension plays an important role in normal contact. Later, Long and Wang [21] addressed the axisymmetric contact between a rigid sphere and an elastic half space with surface tension based on the analytical solution of the literature [14] and concluded that the normal displacement of the elastic half space surface decreases significantly due to the surface tension. Ding et al. [22] analyzed the problem of elastic nanoparticles being compressed by two rigid planes by finite element method. The results show that the compression of an elastic sphere by a rigid plane is equivalent to the indentation of an elastic half space by a rigid sphere, even in the presence of surface tension. In recent years, the influence of surface tension on adhesive contact has also attracted extensive attention. Salez et al. [23] addressed the adhesive contact between a spherical elastic particle and a rigid substrate used a thermodynamical method. Gao et al. [24] studied

the influence of the surface tension on the JKR [25] adhesive contact and first developed a scaling law for pull-off force. The adhesive contact considering surface tension between a rigid sphere and an elastic half space was investigated by the finite element method [26]. Recently, Zhu and Xu [27] revealed more features of adhesive contact by adopting the equivalent system of a rigid sphere and an elastic half space with surface tension.

In the above literature, the ratio of surface tension to equivalent elastic modulus is used to reflect the effect of surface tension on the contact behavior. However, the following details were ignored: (1) in addition to the equivalent of asperities into a sphere and also can be equivalent to conical asperity [28–30]; (2) little work considered the contribution of surface tension on contact characteristics between two rough surfaces; (3) when studying the influences of surface tension on contact characteristics, the influence of surface tension on contact stiffness was not considered, which made theoretical results not accurately reflect the contact characteristics between rough surfaces.

Therefore, in this work, the asperity on the rough surface is equivalent to a cone, and the Nayak's model [31] is adopted to describe the height and curvature distribution of asperities. A single conical asperity system considering the surface tension is built. Furthermore, the model of a single conical asperity system is extended to the entire rough surface based on statistical theory. The effects of surface tension and semi-cone angle of conical asperities on the contact load, the real contact area, and the contact stiffness of the rough surface are revealed.

2 The stochastic process of rough surfaces

Characterizing the height and curvature distribution of asperities reasonably is necessary for studying the contact characteristics of rough surfaces and in the following derivation.

The contact behavior of two rough surfaces can be simplified by the contact between a rigid plane and an equivalent rough surface based on the GW model [3]. Figure 1 shows the schematic of an equivalent rough surface in which the Cartesian coordinate system ($O-xyz$) is built on the mean plane ($z=0$), where z is the height of the asperity, d is the separation between the smooth rigid plane and the mean height plane of the asperity, and F_r is the total load applied to the rough surface.

The auto-correlation function of the rough surface profile is defined as

$$R(x, y) = \lim_{L \rightarrow \infty} \frac{1}{4L^2} \int_{-L}^L \int_{-L}^L z(x_0, y_0) z(x_0 + x, y_0 + y) dx_0 dy_0 \quad (1)$$

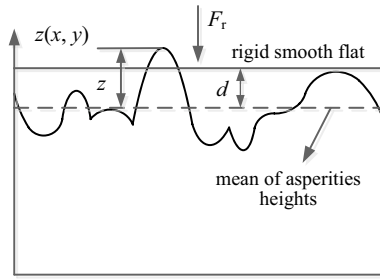


Fig. 1 Schematic of the equivalent rough surface

where $2L$ represents the sampling length.

The power spectral density function of the stochastic process is introduced, which is defined as the Fourier transform of $R(x, y)$

$$\Phi(a, b) = \frac{1}{4\pi^2} \int_{-\infty}^{\infty} \int_{-\infty}^{\infty} R(x, y) \exp[-i(xa + yb)] dx dy \quad (2)$$

where i represents imaginary number, a and b are the number of the wave in the x and y directions, respectively. The moment of $\Phi(a, b)$ can be expressed as

$$m_{pq} = \int_{-\infty}^{\infty} \int_{-\infty}^{\infty} \Phi(a, b) a^p b^q da db \quad (3)$$

We consider an isotropic rough surface with $m_{p0} = m_{0p} = m_p$, where m_p is the moment of the power spectral of the rough surface profile in any direction. According to Eq. (3), we can obtain the moment $m_{00} = m_0 = \sigma^2$, where σ is the standard deviation of the rough surface.

Random variables $(\lambda_1, \lambda_2, \lambda_3, \lambda_4, \lambda_5, \lambda_6)$ are used to characterize random rough surface parameters, and the variables were defined as follows

$$\begin{aligned} \lambda_1 &= z, \quad \lambda_2 = \frac{\partial z}{\partial x}, \quad \lambda_3 = \frac{\partial z}{\partial y}, \quad \lambda_4 = \frac{\partial^2 z}{\partial x^2}, \\ \lambda_5 &= \frac{\partial^2 z}{\partial x \partial y}, \quad \lambda_6 = \frac{\partial^2 z}{\partial y^2} \end{aligned} \quad (4)$$

For a random, isotropic and Gaussian rough surface, Nayak [31] derived the joint probability density with the form of

$$p(\lambda_1, \lambda_2, \lambda_3, \lambda_4, \lambda_5, \lambda_6) = \frac{3\sqrt{3}}{16\pi^3 m_2^2 m_4 \sqrt{(2\alpha - 3)}} \exp\left(-\frac{1}{2}\Theta_1\right) \quad (5)$$

and

$$\begin{aligned} \Theta_1 &= \frac{2\alpha}{2\alpha - 3} \frac{\lambda_1^2}{m_0} + \frac{9(\alpha - 1)}{4(2\alpha - 3)} \frac{\lambda_4^2 + \lambda_6^2}{m_4} + \frac{3\lambda_5^2}{m_4} \\ &+ \frac{3}{(2\alpha - 3)} \frac{\lambda_1(\lambda_4 + \lambda_6)}{m_2} - \frac{3(\alpha - 3)}{2(2\alpha - 3)} \frac{\lambda_4 \lambda_6}{m_4} + \frac{\lambda_2^2 + \lambda_3^2}{m_2} \end{aligned}$$

$$\alpha = \frac{m_0 m_4}{m_2^2} \geq \frac{3}{2} \quad (6)$$

where α is a dimensionless value and m_0, m_2 , and m_4 represent the zero-order spectrum, the second-order spectrum, and the fourth-order spectrum, respectively.

Summit point $z(x, y)$ on the rough surface fulfills

$$\lambda_2 = \lambda_3 = 0, \quad \lambda_4 < 0, \quad \lambda_6 < 0, \quad \lambda_4 \lambda_6 - \lambda_5^2 \geq 0 \quad (7)$$

Therefore, the probability density function for the distribution of a summit with height λ_1 on the entire random rough surface is

$$p_{\text{sum}}(\lambda_1) = \iiint_{\nu} p(\lambda_1, 0, 0, \lambda_4, \lambda_5, \lambda_6) \left| \lambda_4 \lambda_6 - \lambda_5^2 \right| d\lambda_4 d\lambda_5 d\lambda_6 \quad (8)$$

By integrating the probability density function $p_{\text{sum}}(\lambda_1)$ on the range $(-\infty, \infty)$, the density of the summit on the rough surface can be obtained

$$D_{\text{sum}} = \int_{-\infty}^{\infty} p_{\text{sum}}(\lambda_1) d\lambda_1 = \frac{1}{6\pi\sqrt{3}} \frac{m_4}{m_2} \quad (9)$$

The dimensionless height and average curvature of asperities are then

$$\lambda^* = \frac{\lambda_1}{\sqrt{m_0}} = \frac{z}{\sqrt{m_0}}, \quad \rho = \frac{\rho_0}{\sqrt{m_4}} \quad (10)$$

and

$$\rho_0 = \sqrt{\lambda_4 \lambda_6 - \lambda_5^2} \quad (11)$$

where λ^* and ρ represent the dimensionless height and mean curvature of the summit, respectively. ρ_0 is the geometric mean curvature of the summit.

Based on the extension of Nayak's stochastic process theory by Greenwood et al. [32], the probability density function of the asperity with dimensionless height λ^* and dimensionless mean curvature ρ on a random rough surface is obtained

$$\begin{aligned} p_{\text{sum}}(\lambda^*, \rho) &= \frac{m_4}{m_2} \frac{1}{4\pi^{3/2}} \sqrt{\frac{3\alpha}{2(\alpha - 1)}} \rho^3 \\ &\times \exp\left(\frac{3}{2}\rho^2 - \frac{\alpha\lambda^{*2}}{2(\alpha - 1)}\right) \text{erfc}\left(3\eta\rho - \frac{\eta\sqrt{\alpha}}{\alpha - 1}\lambda^*\right) \end{aligned} \quad (12)$$

where $\eta = \sqrt{(\alpha - 1)/(4\alpha - 6)}$ and the error function $\text{erfc}(x)$ is $\text{erfc}(x) = \frac{2}{\sqrt{\pi}} \int_x^{\infty} \exp(-y^2) dy$.

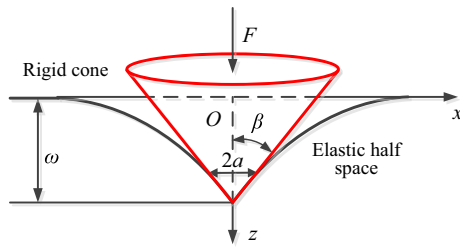


Fig. 2 A rigid equivalent asperity in contact with an elastic half space

3 Contact of single conical asperity

According to the research conclusion of the literature [22], the compression contact between an elastic cone and a rigid plane is also equivalent to the indentation of an elastic half space with surface tension by a rigid cone. In order to simplify the calculation, the latter is considered, and the contact model as shown in Fig. 2. We assume that all the asperities are cones with uniform semi-cone angle β at least near their summits. Thus, the contact of two rough surfaces can be equivalent to the contact of a rigid smooth plane and multiple conical asperities.

The rigid cone contacts the elastic half space and brings about an indent depth ω and a contact half width a when normal load F is applied on the rigid cone along the z -axis. Based on the geometric relation, the normal displacement of the elastic half space surface within the contact area ($r \leq a$) satisfies

$$u(r, 0) = \omega - r \cot \beta \tag{13}$$

When a concentrated force P is applied on the surface of the elastic half space with surface tension, the analytical solution of the normal displacement of the elastic half space surface is obtained by Hajji [14], which can be expressed as

$$u(r, 0) = \frac{P}{4\gamma} \left[H_0\left(\frac{r}{s}\right) - Y_0\left(\frac{r}{s}\right) \right] \tag{14}$$

and

$$s = \frac{2\gamma}{E^*}, \quad E^* = \frac{2G}{1 - \mu} \tag{15}$$

where γ represents the surface tension, E^* is the composite elastic modulus, s represents the elastocapillary length of material, G is the shear modulus, μ is Poisson's ratio, r is the radial distance to the acting point of P , H_0 and Y_0 represent the Struve function and the Bessel function of the second kind (both of order 0).

In this paper, the polar coordinates (t, θ) are introduced to represent the point in the contact region, where t is the distance from a point in the contact region to the contact center and θ indicates the position of the point, as shown in Fig. 3. The contact pressure at point $M(t, \theta)$ is denoted as $p(t)$, while the

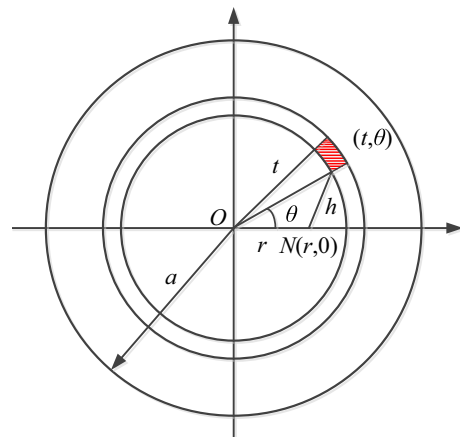


Fig. 3 Schematic of the contact region

pressure applied on a certain element of area $t dt d\theta$ is regarded as a point force $tp(t) dt d\theta$. Therefore, combining Eq. (14), the normal displacement at $N(r, 0)$ caused by the point force $tp(t) dt d\theta$ at point M can be expressed as

$$u_{MN}(r, 0) = \frac{tp(t) dt d\theta}{4\gamma} \left[H_0\left(\frac{h}{s}\right) - Y_0\left(\frac{h}{s}\right) \right] \tag{16}$$

where h is the distance between point M and point N , and $h = \sqrt{r^2 + t^2 - 2rt \cos \theta}$.

Consequently, the normal displacement of point $N(r, 0)$ by the pressure applied to the entire contact area satisfies

$$u(r, 0) = \frac{1}{4\gamma} \int_0^{2\pi} \int_0^a tp(t) \left[H_0\left(\frac{h}{s}\right) - Y_0\left(\frac{h}{s}\right) \right] dt d\theta \tag{17}$$

According to the force balance, the total pressure applied on the entire area should be equal to the normal load F applied on the rigid cone, thus

$$F = \int_0^{2\pi} \int_0^a tp(t) dt d\theta = 2\pi \int_0^a tp(t) dt \tag{18}$$

Substitution of Eq. (17) into (13) gives

$$u(r, 0) = \frac{1}{4\gamma} \int_0^{2\pi} \int_0^a tp(t) \left[H_0\left(\frac{h}{s}\right) - Y_0\left(\frac{h}{s}\right) \right] dt d\theta = \omega - r \cot \beta \tag{19}$$

From Eq. (19), when $r=0$, the indent depth can be expressed as

$$\omega = \frac{\pi}{2\gamma} \int_0^a \left[H_0\left(\frac{t}{s}\right) - Y_0\left(\frac{t}{s}\right) \right] tp(t) dt \tag{20}$$

Taking the first derivative with respect to r through Eq. (19)

$$\frac{1}{2s\gamma} \int_0^{2\pi} \int_0^a \left[H_1\left(\frac{h}{s}\right) - Y_1\left(\frac{h}{s}\right) - \frac{2}{\pi} \right] \frac{r - t \cos \theta}{h} tp(t) dt d\theta = \cot \beta \tag{21}$$

where H_1 and Y_1 are the Struve function and the Bessel function of the second kind (both of order 1).

We use the Gauss–Chebyshev quadrature formula to numerically solve Eqs. (18) and (21). The specific solution flow is shown in Fig. 4.

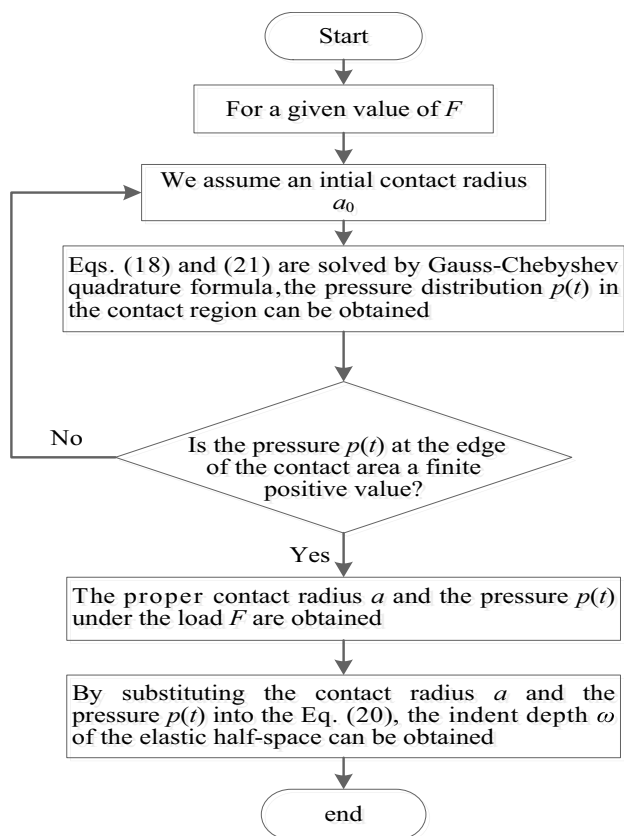


Fig. 4 Flow chart of numerical solution

In the above numerical process, the dichotomy method can be used to obtain the true contact radius. The input parameters are: $\beta = 60^\circ$, $G = 1$ MPa, $\mu = 0.5$, and $\gamma = 0.1$ J/m² [33]. Therefore, it has $s = 50$ nm. Furthermore, the dimensionless contact load $F/F_e(\omega)$ and the dimensionless contact area $A/A_e(\omega)$ can be obtained. By fitting the numerical solution results, the contact load F and real contact area A can be expressed as

$$F = F_e(\omega) \left[1 + 1.1689 \left(\frac{\omega \tan \beta}{s} \right)^{-0.9328} \right] \tag{22}$$

$$F_e(\omega) = \frac{2E^* \omega^2}{\pi \cot \beta} \tag{23}$$

$$A = A_e(\omega) \left[\frac{1 + 0.049 \left(\frac{\omega \tan \beta}{s} \right)^{-1.159}}{1 + 2.429 \left(\frac{\omega \tan \beta}{s} \right)^{-0.8337}} \right] \tag{24}$$

$$A_e(\omega) = \frac{4}{\pi} \omega^2 \tan^2 \beta \tag{25}$$

where $F_e(\omega)$ and $A_e(\omega)$ are, respectively, the results of the classical elastic model solution.

Figure 5a, b indicates the contact load and the real contact area results obtained via the classical elasticity theory, numerical solutions, and predictions by Eqs. (22) and (24), respectively. The results predicted by Eqs. (22) and (24) are in great agreement with the numerical results. At the same time, it is found that as $(\omega \tan \beta)/s$ decreases, the dimensionless contact area $A/A_e(\omega)$ also gradually decreases, but the dimensionless contact load $F/F_e(\omega)$ gradually increases.

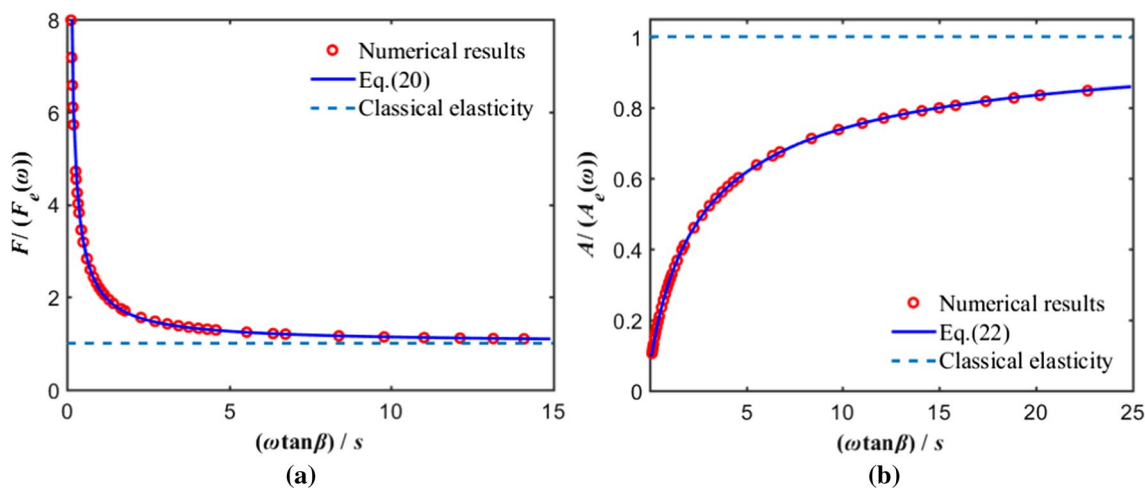


Fig. 5 Variation of contact load and real contact area with indent depth. **a** The normal contact load and **b** the real contact area

In addition, the results from Eq. (22) and the numerical values are gradually approaching the solution of the classical elasticity theory when surface tension is ignored ($(\omega \tan \beta)/s \rightarrow \infty$), where the contact load and real contact area approach the classical elasticity solution. However, the results from the numerical calculations and Eq. (22) deviate from the solution of the classical elasticity theory when the surface tension has a crucial role in contact ($(\omega \tan \beta)/s \rightarrow 0$). It reveals that when the indent depth is small, the surface tension has a significant influence on the joint surface.

The pressure distribution also plays a significant role in contact. Sneddon et al. [34] have addressed the elastic contact model between a rigid cone and an elastic half space without considering the surface tension. The pressure distribution can be written as the inverse hyperbolic cosine function, as follows

$$p(t) = \frac{p}{\pi a^2} \cosh^{-1} \left(\frac{a}{t} \right) \tag{26}$$

where $p/(\pi a^2)$ represents the mean contact pressure.

The pressure distribution in the contact area considering surface tension can be obtained via Eqs. (21) and (18). Figure 6 illustrates the dimensionless pressure distribution for different values of $a/s = 0.2, 2.0,$ and 20 [35]. It is found that the inverse hyperbolic cosine pressure has a natural logarithm singular at the tip of the cone (center of the contact area). Meanwhile, when the ratio of a to s is large, the pressure distribution curve tends to the classical elasticity solution. However, when the ratio of a to s is small, the pressure distribution is obviously different from the classical elastic solution. In this case, the effect of surface tension cannot be ignored. The pressure at the edge of the contact area gradually increases with decreasing ratio of a to s , but the pressure at the central contact area decreases. These results indicate that surface tension makes the pressure distribution more uniform.

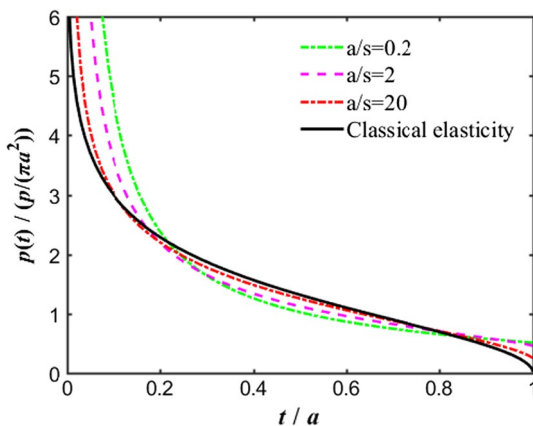


Fig. 6 The distribution of pressure in the contact area

According to the definition of stiffness, the normal contact stiffness of a single conical asperity is defined by

$$k_s = \frac{dF}{d\omega} = k_e(\omega) \left[1 + 0.6238 \left(\frac{\omega \tan \beta}{s} \right)^{-0.9328} \right] \tag{27}$$

$$k_e(\omega) = \frac{4E^* \omega}{\pi \cot \beta} \tag{28}$$

where $k_e(\omega)$ is the solution of the classical elastic model.

Figure 7 shows the trend of the dimensionless normal contact stiffness as a function of the indent depth. The numerical solution results agree well with Eq. (27). The contact stiffness gradually approaches the classical elasticity solution when surface tension approaches zero ($(\omega \tan \beta)/s \rightarrow \infty$). However, the contact stiffness deviates from the classical elastic contact analysis results when the surface tension tends to infinity ($(\omega \tan \beta)/s \rightarrow 0$). With the decrease in $(\omega \tan \beta)/s$, the normal contact stiffness increases, and when $(\omega \tan \beta)/s$ is relatively small, the stiffness increases sharply, owing to the dramatic increase in load with the decrease in $(\omega \tan \beta)/s$.

4 New contact model of rough surface

As can be seen from Fig. 2, the conical asperity is applied a normal load F , and the indent depth of the single conical asperity is $\omega = z - d$. Substituting ω into Eqs. (22), (24), and (27), respectively, the contact load, real contact area, and normal contact stiffness of a conical asperity system can be obtained. Based on the statistical method and the probability density function Eq. (12), the contact load F_r , real contact area A_r , and normal contact stiffness K_n of rough surfaces can be determined by

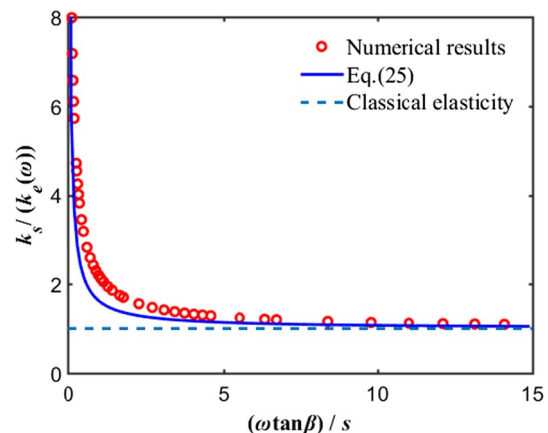


Fig. 7 Normal contact stiffness versus indent depth

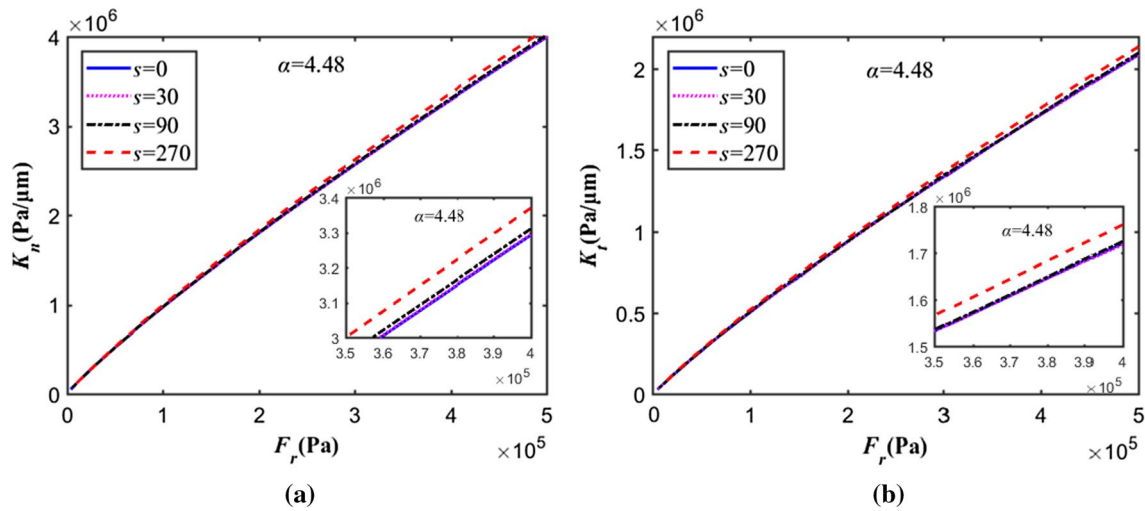


Fig. 8 The contact stiffness as a function of normal contact load for $\alpha=4.48$. **a** The normal contact stiffness and **b** the tangential contact stiffness

$$F_r = \int_0^\infty \int_d^\infty F(z-d)p_{\text{sum}}(z, \rho_0) dz d\rho_0 \tag{29}$$

$$A_r = \int_0^\infty \int_d^\infty A(z-d)p_{\text{sum}}(z, \rho_0) dz d\rho_0 \tag{30}$$

$$K_n = \int_0^\infty \int_d^\infty k_s(z-d)p_{\text{sum}}(z, \rho_0) dz d\rho_0 \tag{31}$$

The relationship between the normal stiffness and the tangential stiffness of rough surfaces can be expressed as [36]

$$\frac{K_t}{K_n} = \frac{C(1-\mu)}{2-\mu} \tag{32}$$

where μ represents the Poisson's ratio of the elastic material, and $C = \pi/2$ [36].

Consequently, the tangential contact stiffness obtained by Eq. (32) is

$$K_t = \frac{\pi(1-\mu)}{2(2-\mu)} K_n \tag{33}$$

Equations (29), (30), (31), and (33) are dimensionless, as follows

$$F_r^* = \frac{m_2 \tan \beta}{\pi^{5/2}} \sqrt{\frac{3\alpha^3}{8(\alpha-1)}} \int_0^\infty \int_u^\infty (\lambda^* - u)^2 \rho^3 \times \left\{ 1 + 1.1689 \left[\frac{(\lambda^* - u) \tan \beta}{s^*} \right]^{-0.9328} \right\} \times \exp \left[\frac{3}{2} \rho^2 - \frac{\alpha \lambda^{*2}}{2(\alpha-1)} \right] \times \operatorname{erfc} \left(3\eta\rho - \frac{\eta\sqrt{\alpha}}{\alpha-1} \lambda^* \right) d\lambda^* d\rho \tag{34}$$

$$A_r^* = \frac{m_2 \tan^2 \beta}{\pi^{5/2}} \sqrt{\frac{3\alpha^3}{2(\alpha-1)}} \int_0^\infty \int_u^\infty (\lambda^* - u)^2 \rho^3 \times \left\{ \frac{1 + 0.049 \left(\frac{(\lambda^* - u) \tan \beta}{s^*} \right)^{-1.159}}{1 + 2.429 \left(\frac{(\lambda^* - u) \tan \beta}{s^*} \right)^{-0.8337}} \right\} \times \exp \left[\frac{3}{2} \rho^2 - \frac{\alpha \lambda^{*2}}{2(\alpha-1)} \right] \times \operatorname{erfc} \left(3\eta\rho - \frac{\eta\sqrt{\alpha}}{\alpha-1} \lambda^* \right) d\lambda^* d\rho \tag{35}$$

$$K_n^* = \frac{\tan \beta}{\pi^{5/2}} \sqrt{\frac{3\alpha^2}{2(\alpha-1)}} \int_0^\infty \int_u^\infty (\lambda^* - u) \rho^3 \times \left\{ 1 + 0.6238 \left[\frac{(\lambda^* - u) \tan \beta}{s^*} \right]^{-0.9328} \right\} \times \exp \left[\frac{3}{2} \rho^2 - \frac{\alpha \lambda^{*2}}{2(\alpha-1)} \right] \times \operatorname{erfc} \left(3\eta\rho - \frac{\eta\sqrt{\alpha}}{\alpha-1} \lambda^* \right) d\lambda^* d\rho \tag{36}$$

$$K_t^* = \frac{\pi(1-\mu)}{2(2-\mu)} K_n^* \tag{37}$$

Table 1 Spectral moments and bandwidth of the rough surface

$m_0/\mu\text{m}^2$	m_2	$m_4/\mu\text{m}^{-2}$	α
0.09	12.04	7225	4.48

where s^* and u are the dimensionless surface tension parameters and the dimensionless separation between the smooth rigid plane and the mean height plane of the asperity, respectively, and $s^* = s/\sqrt{m_0}$, $u = d/\sqrt{m_0}$.

Figure 8 shows the contact stiffness–contact load curves of the rough surface considering the surface tension by using the surface topography parameters in Table 1. It is obvious to find that as the contact load increases, the contact stiffness also increases, and the relationship between the contact stiffness and the load can be approximated as linear. In addition, the contact stiffness is proportional to the surface tension when the load is constant.

5 Verification of model correctness

A bolted joint with two identical rough surfaces is considered for verification. The static stiffness of the bolted joint surface is generally measured by the deformation of the structure under static load, while the dynamic stiffness is measured by the frequency of the structural vibration. However, the static stiffness can be approximated by dynamic stiffness when the excitation frequency is small, especially for values less than 5 Hz. Thus, the finite element model (FEM) is established by the normal and

tangential stiffness obtained in Sect. 4. The data obtained by the finite element model are compared to experimental measurements using the method shown in Fig. 9.

5.1 The finite element model

A schematic diagram of two test pieces in contact with each other under normal load (bolt pre-tightening force) is shown in Fig. 10a. The bolted joint surface is made by connecting part A and part B with two same high-strength steel structural bolts (M16). From Fig. 10b, we can see that the contact characteristics of the bolted joint surface are simulated by normal stiffness K_n , tangential stiffness K_t , normal damping d_n , and tangential damping d_t . The damping of the bolted joint surface will be ignored because the damping only affects the amplitude of the resonance and has no significant influence on other model parameters.

Then, the overall stiffness model of the bolted joint surface considering surface tension can be expressed as

$$K_i = \begin{bmatrix} K & 0 & K & 0 \\ 0 & K & 0 & K \\ K & 0 & K & 0 \\ 0 & K & 0 & K \end{bmatrix} \tag{38}$$

where $K = \begin{bmatrix} K_n & 0 \\ 0 & K_t \end{bmatrix} = \begin{bmatrix} K_x & 0 & 0 \\ 0 & K_y & 0 \\ 0 & 0 & K_z \end{bmatrix}$ (39)

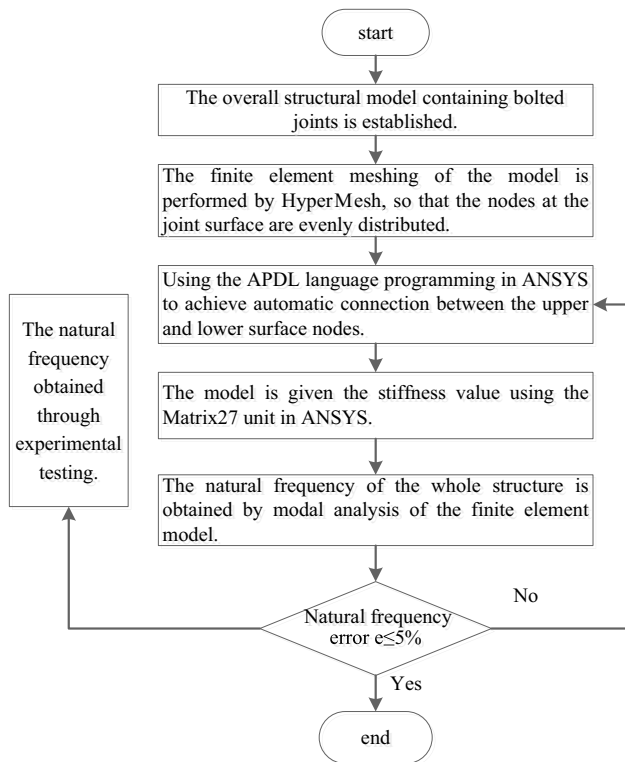


Fig. 9 Verification method of the whole model

In this paper, we first create a three-dimensional model of the bolted joint as shown in Fig. 11a and finite element meshing of the model is divided by Hypermesh software. Then, the model is imported into ANSYS16.0 with the assumption that the joint surface nodes are connected by springs and dampers (as shown in Fig. 11b) for simplification. An automatic program is written through the APDL language to connect the nodes. The Matrix27 element is

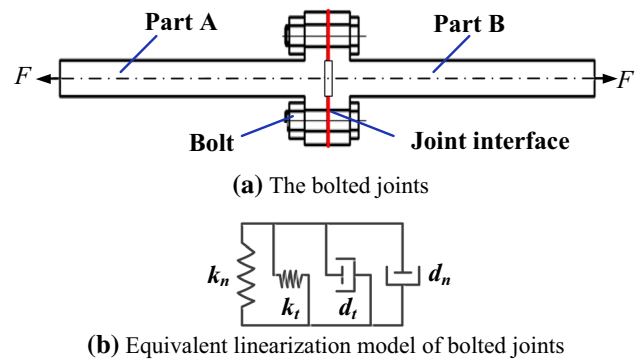


Fig. 10 The bolted joints and their mathematical idealization

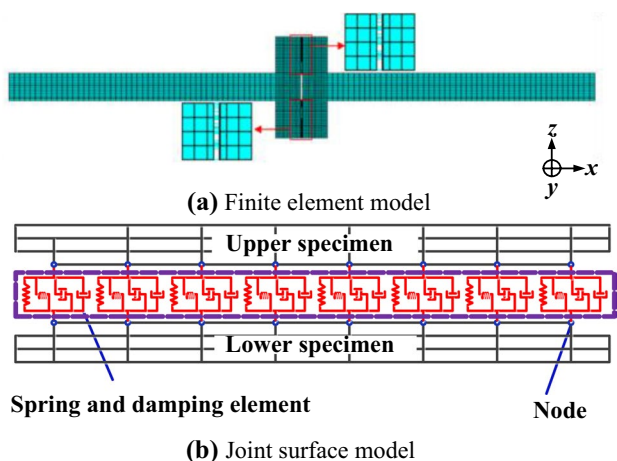


Fig. 11 Finite element model of whole structure

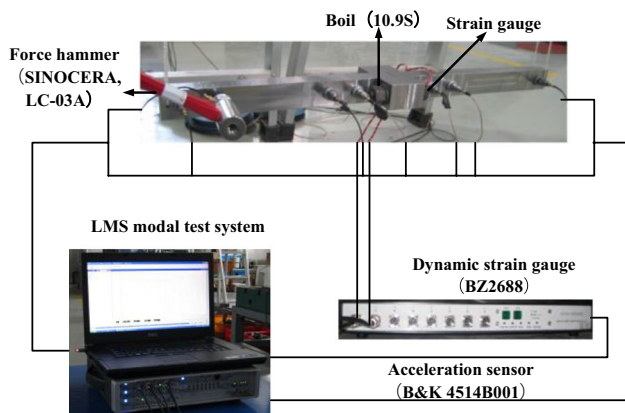


Fig. 12 Experimental principle of model characteristics

used to simulate the equivalent dynamics of the bolted joint [37]. The stiffness parameter obtained by Eq. (38) is brought into the finite element model for modal analysis to obtain the frequency response function of the overall structure.

5.2 Test procedure

The experimental platform was built as shown in Fig. 12. The system consists of test pieces, the LMS modal test system, high-strength bolts, dynamic strain gauges, force hammers (SINOCERA, LC-03A), and acceleration sensors (B&K, 4514B001). Two test pieces are connected by high-strength bolts with the dynamic strain gauges built to measure the bolt pre-tightening force. The acceleration sensor can acquire an acceleration signal at the selected position when the force hammer applies a vibration load. The frequency range was selected from 0 to 1800 Hz, the frequency sampling was 2 Hz, and the bolt pre-tightening force was 30 kN. During the experiment, the test piece was continuously knocked 10 times, and the knocking force was basically the same. The LMS modal test analysis instrument was used to collect and analyze the input signal and the response signal, and the average value of the test was taken 10 times to reduce noise interference. The frequency response function of the whole structure is obtained by applying the H1 algorithm to the collected force signal and acceleration signal.

Figure 13a, b compares the modal test results and finite element simulation results of frequency response functions $H(1, 1)$ and $H(1, 2)$. It is known that the frequency response functions obtained by finite element simulation and the modal test are consistent. However, the results of paper's model are closer to the modal test results, which illustrates that the proposed model is more reasonable. In addition, the first three-order natural frequencies obtained by the modal

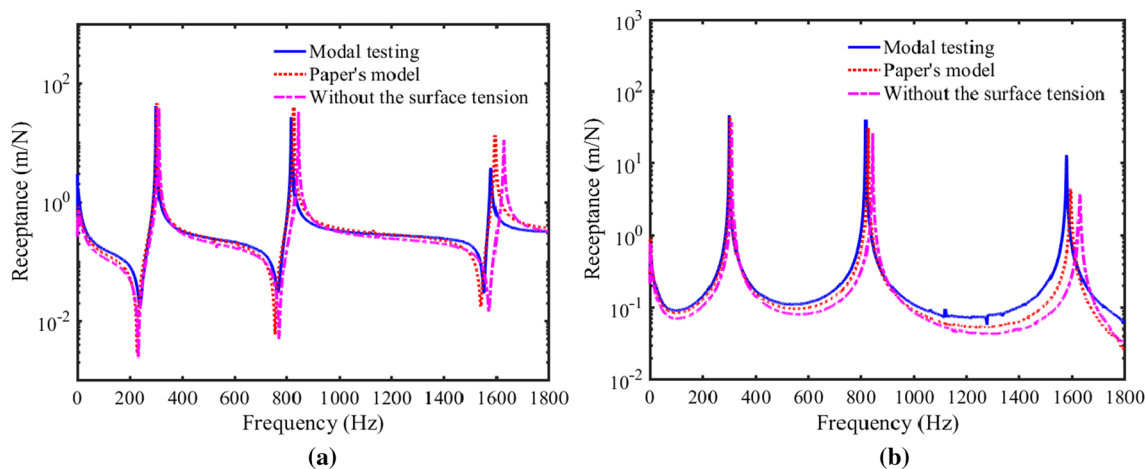


Fig. 13 The results of modal testing and the finite element results for $p=30(kN)$. **a** FRF ($H(1, 1)$) and **b** FRF ($H(1, 2)$)

test are 301 Hz, 818 Hz, and 1581 Hz, respectively, and the results of paper’s model considering surface tension are 307 Hz, 835 Hz, and 1612 Hz, respectively, while the finite element results without the surface tension are 312 Hz, 854 Hz, and 1658 Hz, respectively. The modal test data are regarded as accurate, and after the natural frequency of the modal test is compared with the results of paper’s model, the errors of the first three-order natural frequencies are 1.99%, 2.08% and 1.20%, respectively, which are less than 5%. Meanwhile, the natural frequency of the modal test is compared with the finite element results without the surface tension, yielding errors of 3.65%, 3.91%, and 4.36%, respectively, which are also less than 5%.

6 Results and analysis

As indicated in Fig. 12, the samples selected in this paper and the surface topography of the samples are measured using a Talysurf surface profiler with a resolution of 0.25 μm. The parameters obtained are shown in Table 1.

To illustrate the effect of surface tension, the suitable elastocapillary lengths are reasonably chosen as $s=0, 30, 90, 270$ nm based on the analysis in [33], and when the bandwidth parameter $\alpha=4.48$, the dimensionless surface tension parameters $s^*=0, 0.1, 0.3, 0.9$. The dimensionless separation u is from 1.5 to 3.5 [38].

6.1 Contact characteristics of rough surfaces with different surface tension

In Sect. 3, all asperities on the rough surface are assumed as cones with a semi-cone angle β at least near their summits. In this section, we set $\beta=60^\circ$ and $s=0, 30, 90, 270$ nm, respectively.

Figure 14a, b shows the contact load and the real contact area as a function of dimensionless separation for four values of $s=0, 30, 90, 270$ nm. It is found that variation of the load and the real contact area with the dimensionless separation agrees well with the classical elasticity solution for the case $s=0$, which verifies the correctness of the proposed model. Both the normal load and the real contact area increase with the decreasing of dimensionless separation. This is because the real contact area increases with the decrease in the dimensionless separation, and the contact load also increases accordingly. At the same time, when the dimensionless separation is constant, the contact load increases as the surface tension increases, while the real contact area decreases. It indicates that the proposed model has a larger contact load, but a lower real contact area than the classical elasticity model. This can be attributed to the reason that the surface tension prevents contact with rough surfaces, resulting in lower real contact area and larger contact load. Finally, as the amplitude of surface tension increases, the rate of contact load increase is also increasing, as well as the rate at which the real contact area decreases.

Figure 15 shows the contact stiffness as a function of dimensionless separation for four values of $s=0, 30, 90, 270$ nm. In this case, we observe that the contact stiffness shows the same trend as the contact load in Fig. 14a, which can be attributed to the reason that the number of asperity contacts increases and the real contact area increases when the dimensionless separation decreases. Therefore, the contact stiffness also increases. It is noteworthy that the normal contact stiffness and tangential contact stiffness calculated by the presented model agree well with the classical elasticity solution when the surface tension is neglected ($s=0$). Also, as expected the normal contact stiffness and tangential contact stiffness with the surface tension increases will be larger than predicted by the classical elasticity model. It

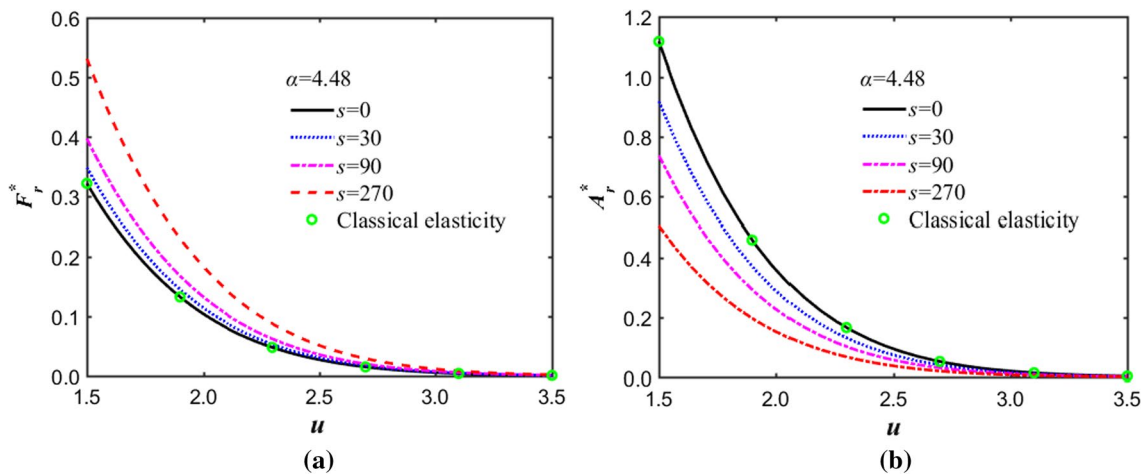


Fig. 14 Variation of contact load and real contact area with separation in different surface tension values for $\alpha=4.48$. **a** The normal contact load and **b** the real contact area

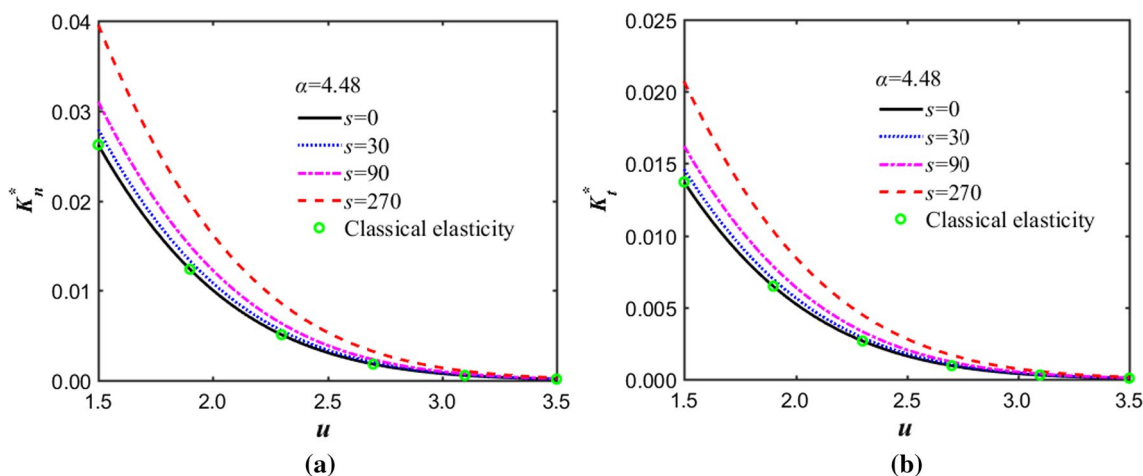


Fig. 15 The relation curve between the contact stiffness and separation with different surface tension values for $\alpha=4.48$. **a** The normal contact stiffness and **b** the tangential contact stiffness

can be also concluded that the surface tension has a critical influence on the study of the contact characteristics between two rough surfaces. Furthermore, for a specific value of dimensionless separation, the contact stiffness increases as the surface tension increases, and the rate of contact stiffness increase is also increasing with rise in surface tension amplitude.

6.2 Contact characteristics of joint surfaces with different semi-cone angles

In the above study, all asperities are equivalent to a cone with a semi-cone angle of 60° , but actually the cone angle of the asperity has an important influence on studying the characteristics of rough surfaces, which is investigated on the contact characteristics of rough surfaces as follows: we

take the elastocapillary length $s = 50$ nm and four samples of $\beta = 15^\circ, 30^\circ, 45^\circ, 60^\circ$. Figure 16a, b shows the contact load and the real contact area as a function of dimensionless separation with different semi-cone angles, respectively. It can be seen from Fig. 16a that when the dimensionless separation u is constant, a larger semi-cone angle of the asperity corresponds to a greater contact load. The reason is that the increase in semi-cone angle of the asperity leads to the increases in real contact area. However, this trend is weakening as the dimensionless separation u increases. As illustrated in the Fig. 16b, under a constant dimensionless separation, the larger the semi-cone angle is, the larger the real contact area will be and the more obvious the change in the real contact area. In addition, it is found that the real contact area tends to vanish at

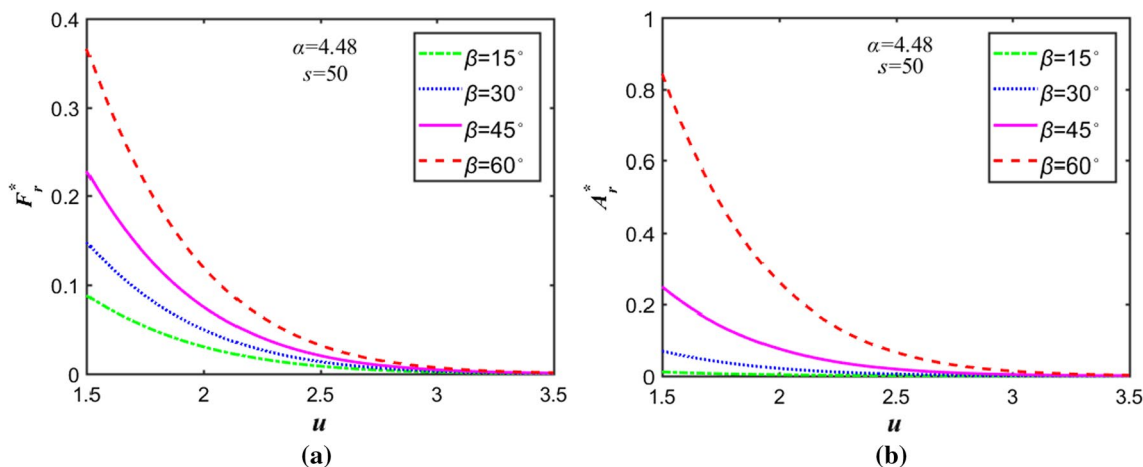


Fig. 16 Variation of contact load and real contact area with separation at different cone angles for $\alpha=4.48$. **a** The normal contact load and **b** the real contact area

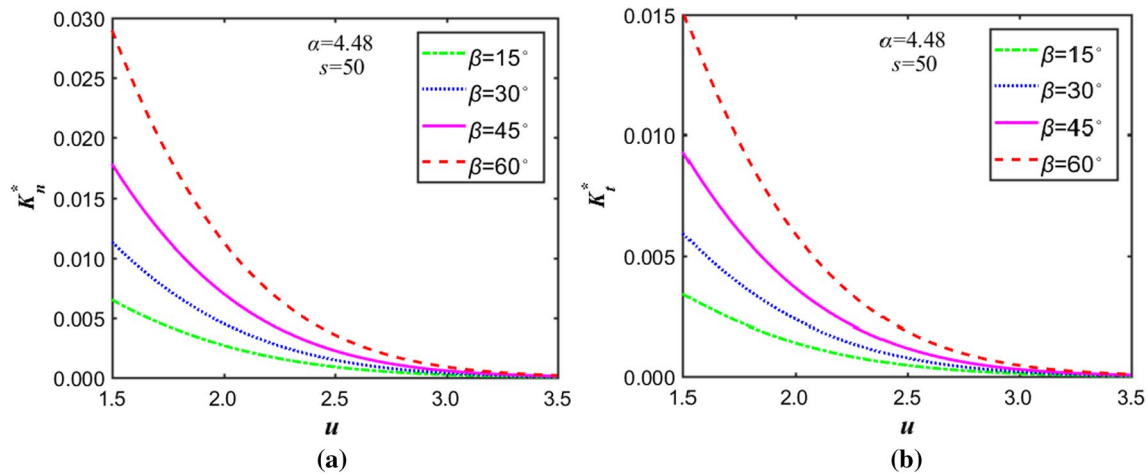


Fig. 17 The relation curve between the contact stiffness and separation at different cone angles for $\alpha=4.48$. **a** The normal contact stiffness and **b** the tangential contact stiffness

$\beta=15^\circ$, but the real contact area is larger at $\beta=60^\circ$, which indicates that a larger semi-cone angle should be selected.

Figure 17a, b shows the normal contact stiffness and the tangential contact stiffness as a function of dimensionless separation for different values of $\beta=15^\circ, 30^\circ, 45^\circ$, and 60° , respectively. As illustrated in Fig. 17a, when the dimensionless separation is fixed, the increase in the semi-cone angle for the asperity enhances the normal contact stiffness, which can be explained by the fact that when the semi-cone angle of the asperity increases, the real contact area between the two rough surfaces increases. In addition, the influence of the semi-cone angle for the asperity on the tangential contact stiffness of rough surface is consistent with its influence on normal contact stiffness in the presence of surface tension, and the normal stiffness is approximately twice the tangential contact stiffness.

7 Conclusions

The influence of surface tension on the contact of rough surfaces should not be ignored since the contact between two rough surfaces happens at some discrete micro/nanoscale spots. In this work, the Nayak's stochastic process model is introduced to describe the isotropic rough surfaces. A new rough surface contact model considering surface tension is established based on statistical theory. The effects of surface tension on the contact characteristics of rough surfaces have been revealed. According to the results, the following conclusions can be drawn.

1. Based on a series of numerical calculations, the explicit relations of contact load, real contact area, and contact stiffness with the indent depth for the single conical asperity system considering surface tension are derived, respectively.

The expressions presented here can be employed to quickly analyze the contact behavior between two rough surfaces. It is noteworthy that the influence of surface tension on contact stiffness is analyzed, which provides theoretical guidance for accurately predicting the dynamic characteristics of rough joint surfaces.

2. The pressure distribution in the contact area depends on the ratio of the contact radius a to the elastocapillary length s of the material. With a larger value of a/s , the pressure distribution curve tends to the classical elasticity solution. Otherwise, it evidently deviates from the classical solution. In this case, the influence of surface tension should not be ignored. More importantly, the pressure at the edge of the contact area gradually increases as the value of a/s decreases, while the pressure at the central contact area decreases, which indicates that the surface tension makes the pressure distribution more uniform.
3. For a particular value of the separation, the new model of rough surface has a larger contact load, larger contact stiffness, and a smaller real contact area, compared to the classical elastic model without the surface tension. This shows that the presence of surface tension causes an increase in mean contact pressure in the contact area.
4. When the surface tension is fixed, the greater the semi-cone angles of the asperity, the greater the contact load, the real contact area, and the contact stiffness will be. The surface roughness can be characterized by the semi-cone angles of the asperity to some extent. For a lower value of the semi-cone angle ($\beta=15^\circ$), it means that the surface roughness is larger, which causes the real contact area of rough surfaces tends to vanish.

Acknowledgements This work was supported by the National Natural Science Foundation of China (Project No. 51305327, 51475352) and the Shaanxi Provincial Natural Science Foundation of China (Project No. 2018JM5066).

References

1. Madhusudana CV (2014) Thermal contact conductance. Springer, Berlin
2. Yovanovich MM (2005) Four decades of research on thermal contact, gap, and joint resistance in microelectronics. *IEEE Trans Compon Packag Technol* 28(2):182–206
3. Greenwood JA, Williamson JP (1966) Contact of nominally flat surfaces. *Proc R Soc Lond A* 295(1442):300–319
4. Chang WR, Etsion I, Bogy DB (1987) An elastic–plastic model for the contact of rough surfaces. *J Tribol* 109(2):257–263
5. Majumdar A, Bhushan B (1991) Fractal model of elastic–plastic contact between rough surfaces. *J Tribol* 113(1):1–11
6. Yuan Y, Gan L, Liu K, Yang X (2017) Elastoplastic contact mechanics model of rough surface based on fractal theory. *Chin J Mech Eng* 30(1):1–9
7. Sepehri A, Farhang K (2009) Closed-form equations for three dimensional elastic–plastic contact of nominally flat rough surfaces. *J Tribol* 131(4):041402
8. Gorbatiikh L, Popova M (2006) Modeling of a locking mechanism between two rough surfaces under cyclic loading. *Int J Mech Sci* 48(9):1014–1020
9. Gerberich WW, Tymiak NI, Grunlan JC, Horstemeyer MF, Baskes MI (2002) Interpretations of indentation size effects. *J Appl Mech* 69(4):433–442
10. Lim CW, Li ZR, He LH (2006) Size dependent, non-uniform elastic field inside a nano-scale spherical inclusion due to interface stress. *Int J Solids Struct* 43(17):5055–5065
11. Huang ZP, Sun L (2007) Size-dependent effective properties of a heterogeneous material with interface energy effect: from finite deformation theory to infinitesimal strain analysis. *Acta Mech* 190(1–4):151–163
12. Ru CQ (2009) Size effect of dissipative surface stress on quality factor of microbeams. *Appl Phys Lett* 94(5):051905
13. Gurtin ME, Murdoch AI (1975) A continuum theory of elastic material surfaces. *Arch Ration Mech Anal* 57(4):291–323
14. Hajji MA (1978) Indentation of a membrane on an elastic half space. *J Appl Mech* 45(2):320–324
15. Huang GY, Yu SW (2007) Effect of surface elasticity on the interaction between steps. *J Appl Mech* 74(4):821–823
16. He LH, Lim CW (2006) Surface green function for a soft elastic half-space: influence of surface stress. *Int J Solids Struct* 43(1):132–143
17. Cuenot S, Frégnigny C, Demoustier-Champagne S, Nysten B (2004) Surface tension effect on the mechanical properties of nanomaterials measured by atomic force microscopy. *Phys Rev B* 69(16):165410
18. Wang GF, Feng XQ (2007) Effects of surface stresses on contact problems at nanoscale. *J Appl Phys* 101(1):013510
19. Olsson PA, Park HS (2012) On the importance of surface elastic contributions to the flexural rigidity of nanowires. *J Mech Phys Solids* 60(12):2064–2083
20. Gao X, Hao F, Fang D, Huang Z (2013) Boussinesq problem with the surface effect and its application to contact mechanics at the nanoscale. *Int J Solids Struct* 50(16–17):2620–2630
21. Long JM, Wang GF (2013) Effects of surface tension on axisymmetric Hertzian contact problem. *Mech Mater* 56(1):65–70
22. Ding Y, Niu X, Wang G (2015) Elastic compression of nanoparticles with surface energy. *J Phys D Appl Phys* 48(48):485303
23. Salez T, Benzaquen M, Raphaël É (2013) From adhesion to wetting of a soft particle. *Soft Matter* 9(45):10699–10704
24. Gao X, Hao F, Huang Z, Fang D (2014) Mechanics of adhesive contact at the nanoscale: the effect of surface stress. *Int J Solids Struct* 51(3–4):566–574
25. Johnson KL, Kendall K, Roberts AD (1971) Surface energy and the contact of elastic solids. *Proc R Soc Lond Math Phys Sci* 324(1558):301–313
26. Xu X, Jagota A, Hui CY (2014) Effects of surface tension on the adhesive contact of a rigid sphere to a compliant substrate. *Soft Matter* 10(26):4625–4632
27. Zhu X, Xu W (2018) Effect of surface tension on the behavior of adhesive contact based on Lennard-Jones potential law. *J Mech Phys Solids* 111:170–183
28. Do M, Cerezo V, Beaudry Y, Kane M (2013) Modeling of the connection road surface microtexture/water depth/friction. *Wear* 302(1–2):1426–1435
29. Hisakado T, Suda H (1999) Effects of asperity shape and summit height distributions on friction and wear characteristics. *Wear* 225:450–457
30. Jourani A (2015) A new three-dimensional numerical model of rough contact: influence of mode of surface deformation on real area of contact and pressure distribution. *J Tribol* 137(1):011401
31. Nayak PR (1971) Random process model of rough surfaces in plastic contact. *Wear* 26(3):398–407
32. Greenwood JA (2006) A simplified elliptic model of rough surface contact. *Wear* 261(2):191–200
33. Shenoy V, Sharma A (2001) Pattern formation in a thin solid film with interactions. *Phys Rev Lett* 86(1):119–122
34. Sneddon IN (1948) Boussinesq’s problem for a rigid cone. *Proc Camb Philos Soc* 44(4):492–507
35. Long J, Ding Y, Wang G (2017) Contact problems at micro/nano scale with surface tension. *Proc IUTAM* 21:40–47
36. Sherif HA, Kossa SS (1991) Relationship between normal and tangential contact stiffness of nominally flat surfaces. *Wear* 151(1):49–62
37. Guo T, Li L, Zhao Y (2012) Alternative method for identification of the dynamic properties of bolted joints. *J Mech Sci Technol* 26(10):3017–3027
38. Popov VL (2010) Contact mechanics and friction. Springer, Berlin

Publisher’s Note Springer Nature remains neutral with regard to jurisdictional claims in published maps and institutional affiliations.